Distributional correspondence of 94-GHz radar reflectivity with the variation in water cloud properties over the northwestern Pacific and China

Kazuaki Kawamoto*

Graduate School of Fisheries Science and Environmental Studies, Nagasaki University, Nagasaki, Japan

Kentaroh Suzuki

Jet Propulsion Laboratory, California Institute of Technology, Pasadena, California, USA

*Corresponding author address: Kazuaki Kawamoto, Graduate School of Fisheries Science and Environmental Studies, Nagasaki University, 1-14 Bunkyo-machi, Nagasaki, Japan 852-8521.

E-mail: kazukawa@nagasaki-u.ac.jp

ABSTRACT

This paper studied the behavior of 94-GHz radar reflectivity (Z_e) with variation in the properties of low-level water clouds, such as the effective droplet radius (r_e), geometrical thickness (D_{cld}), and liquid water path (LWP), over the northwest Pacific and China. The changes in the distribution of maxZ_e (the largest Z_e within a cloud layer) were examined in terms of variation in the cloud parameters such as small, mid and large categories. While maxZ_e had monomodal distributions regarding variation in r_e and D_{cld}, that appeared bimodal in the small category of LWP. It was confirmed that the small category of LWP contained both non-precipitating clouds in the incipient stage and raining clouds in the dissipating stage. Next, optically-measured particle size was combined with LWP derived from the microwave measurement to classify the precipitation type. Applying maxZ_e and D_{cld} to the analysis of classified precipitation types corroborated the importance of D_{cld} for examining the occurrence of precipitation. Finally, the position of maxZ_e relative to the cloud top was investigated using a measure of the probability of precipitation (POP) according to variation in r_e. The results showed that the Pacific and China had 'bow' and 'funnel' shapes, respectively. The emergence of these shapes according to the variation in r_e was interpreted as the enhancement of Z_e due to droplet collisional growth and the attenuation of Z_e by the presence of large particles. Furthermore, a detailed analysis of smaller particles (<10 μm in radius) reinforced the idea of rapid, efficient particle growth in the lower part of the cloud.

1 Introduction

Clouds play several critical roles in maintaining and altering the Earth's climate, such as in radiation and hydrological processes [1]. In addition, increased diffuse radiation increases the efficiency of photosynthesis under cloudy conditions. For example, even small changes in the macrophysics (the areal extent, temporal frequency, height, geometrical thickness, and total amount of water) and the microphysics (particle size, number concentration, and mass density of water or ice particulates) can significantly alter the radiation budget and water cycle of the Earth. Aerosol indirect effects of the first kind [2] and the second kind [3], which involve changes in radiative properties and precipitation efficiency, respectively, have been studied through observations [4–5] and modeling [6–7]. This study mainly considers the observational aspect with satellite sensors.

Clouds are composed of water-, ice- and mixed-phase particles according to the temperature and the history of the formation of the cloud particles. Although it has been almost three decades since Randall et al. [8] pointed out that water clouds were climatically important due to their radiative role and less complicated than ice- and mixed-phase clouds, the water cloud-related problems as mentioned above are far from resolved [9]. Therefore, this study addresses only water clouds with a top temperature warmer than 273 K, and clouds signify low-level water clouds in the rest of this paper.

For almost a decade after the mid-1990s, passive remote sensing of cloud and aerosol properties was performed using Advanced Very High Resolution Radiometer (AVHRR) data. Han et al. [10] first succeeded in a near-global survey of particle size of

water clouds. Nakajima and Nakajima [11] and Kawamoto et al. [12] later conducted detailed regional and global analyses of both optical depth and the particle radius of water clouds. During this time period, Higurashi and Nakajima [13] conducted the first global analysis of aerosol optical depth and the particle size index, but measurements were made only over ocean because the reflection function over land was too uncertain to retrieve aerosol properties accurately. With these processes, thus Nakajima et al. [14] combined the cloud properties from Kawamoto et al. [12] and the aerosol properties from Higurashi and Nakajima [13] and completed the first global survey of aerosol–cloud interaction over ocean with AVHRR data. Soon after this analysis, Bréon et al. [15] used the Polarization Directionality of the Earth's Reflectivity (POLDER) device to globally depict aerosol–cloud interaction over both land and ocean. Regardless of the use of different data sets, both analyses yielded a similar tendency on the aerosol–cloud interaction (similar slope value of the change in cloud droplet radius according to the aerosol index) over the ocean.

Not only remote sensing measurements using shortwave channels such as visible and infrared wavelengths but also those combining passive microwave observations with shortwave have been made to date. Lin and Rossow [16] extracted the ice–water path (IWP) of oceanic cold non-precipitating clouds by taking the difference between the total water path retrieved from the International Satellite Cloud Climatology Project (ISCCP) and liquid water path (LWP) obtained from the Special Sensor Microwave Imager (SSM/I) data. Then Lin and Rossow [17] revealed the seasonal variation of LWP and IWP on a global scale, extending the method of Lin and Rossow [16].

Meanwhile, Lin et al. [18] used the optical (visible, near infrared, and infrared) and microwave measurements to estimate the frequency of multilayered clouds and the particle size of water clouds. Subsequently, Ho et al. [19] applied this method of Lin et al. [18] to data sets from the TRMM Microwave Imager (TMI) and the Visible and Infrared Scanner (VIRS) on the Tropical Rainfall Measuring Mission (TRMM) to examine the frequencies of single-layered/overlapping non-precipitating clouds, and water paths of ice and water clouds. Their result proved the advantage of observing clouds using different sensors on the same platform. Moreover, to retrieve multilayered cloud properties, Huang et al. [20] developed a method combining satellite visible and infrared radiances and surface microwave radiometer measurements. Applying this method, they found that ice-cloud height derived from traditional single-layer retrieval was underestimated, and the midlevel ice cloud coverage was over classified.

However, conventional passive remote sensing techniques have a limitation with regard to vertically resolved measurements. The visible and near-infrared channels can only retrieve the column-integrated optical depth and particle size near the cloud top [21]. In 2006, the CloudSat satellite deployed the Cloud Profiling Radar (CPR) at 94-GHz, which can provide vertical cloud information. Combining the CPR data with data from passive instruments such as the Moderate Resolution Imaging Spectroradiometer (MODIS), new findings have been obtained [22–25]. This type of synergistic analysis combining passive and active sensing techniques has become available because of the advent of the A-Train constellation [1].

Taking this synergetic approach and using CloudSat and MODIS data, Nakajima et

al. [26] proposed a new diagram called the contoured frequency by optical depth diagram (CFODD), which used radar reflectivity as the horizontal axis and in-cloud optical depth as the vertical axis. Using this diagram, Suzuki et al. [27] obtained new insights into the cloud–rain transition processes. These progresses in observations of clouds provide certain new tools in analyzing aerosol effects and in modeling the effect of low level water clouds on global hydrological cycle. Considerable efforts have been made to merge satellite observations with modeling studies to identify and mitigate the model biases. For example, Suzuki et al. [28] undertook a synergistic analysis using CloudSat and MODIS data to evaluate global and regional cloud-resolving models in the context of their representations of the cloud-to-rain conversion processes. More recently, Suzuki et al. [29] focused on the aerosol indirect effect in a global high-resolution model by comparing their outputs with joint CloudSat and MODIS observations to expose fundamental model biases in representing the aerosol indirect effect of the second kind. Recently, Kawamoto and Suzuki [30] performed two types of analyses on the relationships between the radar reflectivity and clouds parameters. One was the probability distribution function of cloud parameters as a function of radar reflectivity, and the other was the fractional occurrence of the precipitation categories as a function of the cloud parameters over the mid-latitude land and ocean. Nevertheless, the current level of understanding on the cloud droplet transition and precipitation formation inside clouds is insufficient.

Under the above-mentioned circumstances, this study was performed with the following two objectives to enhance understanding of the behavior of radar reflectivity

with the variation in water cloud properties using the collocated MODIS and CloudSat products. One was to examine the difference in the distribution of radar reflectivity with the variation in water cloud properties. This examination will reveal the information content on precipitation in cloud properties. The other was to investigate the change in the vertical position of radar reflectivity inside the cloud layer with the variation in water cloud properties. In this way, the change in relative position of the precipitation occurrence in a normalized cloud layer will be determined.

In the remainder of this paper, Section 2 describes the data sets used in this study and Section 3 presents the results of the two analyses. Finally, Section 4 summarizes the overall conclusions.

2. Used data sets

To achieve the purpose of this study, the effective particle radius (r_e), geometrical thickness (D_{cld}), LWP, and radar reflectivity (Z_e) were taken from collocated CloudSat and MODIS data sets for JJA and DJF from 2006 to 2010. The data sources for the used cloud parameters were as follows: 2B-GEOPROF for the vertical distribution of Z_e and cloud mask [31, 32] and D_{cld} estimated from Z_e; 2B-TAU for the optical depth τ and r_e (using the 2.15-μm band) near the cloud top derived from MODIS radiances [33]; 2C-PRECIP-COLUMN for the LWP derived from the microwave measurement discussed in Section 3.2 [34]; ECMWF-AUX for meteorological profiles from the European Center for Medium-Range Weather Forecasts (ECMWF) objective archives [35]. LWP was derived from the following equation [36, 37]:

$$LWP = 5\,\tau r_e / 9 \quad (1).$$

In this study, following Kawamoto and Suzuki [30], the northwestern Pacific and China were selected as analysis areas, as shown in Fig. 1, due to the comparison of the ocean and land at the same latitude. Only single-layered water clouds were analyzed to reduce the uncertainty and complexity associated with multi-layered clouds. The definition of the single-layered water clouds is the same as in Kawamoto and Suzuki [25, 30].

3 Results and discussion

3.1 Correspondence of Z_e to the variation of cloud properties

The maximum Z_e (maxZ_e) is defined as the largest radar reflectivity within a cloud layer and it serves as an indicator of whether or not precipitation occurs in that cloud layer. One of the purposes of this study was to determine how the maxZ_e would react to the variation of the cloud parameters of concern. To achieve this, the quantity of each parameter was divided into the following three categories: small (sml), medium (mid), and large (lrg), and then the frequency distribution of maxZ_e was calculated for all categories of each parameter. The ranges of all categories of each parameter are summarized in Table 1. These ranges were set so that the number in each category was roughly the same for each target area.

First, we describe the characteristics of the probability distribution function (PDF) of the parameters over the target areas. In this study, the effective particle radius (r_e),

geometrical thickness (D_{cld}), liquid water path (LWP), and radar reflectivity (Z_e) were analyzed. The PDFs of r_e in Figure 2 revealed that the Pacific had a monomodal distribution with a mode value of about 20 μm, whereas China had a bimodal distribution with mode values of about 12 and 23 μm. The PDFs of D_{cld} in Figure 3 indicated that the distributions were similar between the two areas. Clouds with a thickness of approximately 500 m are overwhelming, and another three modes can be observed at thicknesses of around 2000, 3500, and 4000 m. For the PDFs of LWP, shown in Figure 4, the distributions were monomodal in both areas, indicating the presence of more water in the Pacific. Finally, Figure 5 shows the PDFs of Z_e. The Pacific had a distinct peak at about 5 dBZ, whereas China exhibited a bimodal distribution with peaks around -20 and 5 dBZ. In this study, Z_e values were used to classify clouds into non-precipitating (Z_e < -15 dBZ), drizzle (-15 < Z_e <0 dBZ; a rain rate of less than 0.03 mm/h) and precipitating (0 dBZ < Z_e), following Suzuki et al. [28] that was adapted from precipitation flags defined in Haynes et al. [34].

Next, the changes in the maxZ_e distribution for different categories of each parameter were investigated to obtain a better understanding of the variation in precipitation characteristics. Figures 6, 7, and 8 show the distributions of maxZ_e according to the three categories of r_e, D_{cld}, and LWP, respectively. In each figure, (a) and (b) represent the Pacific and China cases, respectively. Generally, for r_e in Figure 6, the sml and lrg categories had peaks at the small (about -20 dBZ) and large (about 10 dBZ) reflectivity values, respectively. The mid-category had a flat shape that was intermediate between the sml and lrg categories.

As with the r_e values shown in Figures 6 (a) and (b), the shape of the curves for D_{cld} were monomodal for both the Pacific and China, as shown in Figures 7 (a) and (b). There were peaks in the smaller (-20 dBZ) and larger (10 dBZ) Z_e for the sml and lrg categories, respectively. The Pacific displayed slightly higher frequency around 10 dBZ for the lrg category. In China, smaller Z_e values were more frequent than in the Pacific for the mid-category.

For the LWP, as shown in Figures 8(a) and (b), it is interesting to note that bimodal structures were observed in the range of -20 to 15 dBZ for the sml category in both areas. Although the frequency in the larger mode was higher in the Pacific, in the smaller mode it was almost identical in both areas. In the mid-category, China had a distinct peak at -20 dBZ, but no sharp peak occurred in the Pacific throughout the Z_e range. Alternatively, for the lrg category, in the Pacific a distinct peak occurred at 10 dBZ. The bimodal structures observed in the sml category were analyzed in more detail and discussed subsequently.

For this purpose, Figures 9 (a) and (b) shows the PDFs of r_e in terms of the three LWP categories. The distribution of the sml category in both areas was bimodal, with higher frequencies at the larger r_e mode in the Pacific and the smaller r_e mode in China. Additionally, the mid and lrg categories displayed monomodal distributions, with larger r_e modes in the lrg category for both areas.

Confirming the r_e distribution in each LWP category, the sml categories of LWP in Figures 9(a) and (b) were resolved in terms of the r_e category in Figures 10(a) and (b). From the figures, it is clear that small particles contributed most to the non-precipitating

Z_e region (less than -20 dBZ), whereas medium and large particles contributed most to the precipitating Z_e region (more than 10 dBZ). The above analyses confirmed that the sml category of LWP contained two different types of cloud. These were the initial stage of non-precipitating clouds (smaller r_e and Z_e peaks), and raining clouds in their dissipating stage, when most cloud water had already been lost (larger r_e and Z_e peaks). Moreover, the latter clouds had thin optical depth, low droplet number density, high cloud-top height, and thick geometrical depth. Their mode values were approximately 2.5, 10 cm^{-3}, 5000 m, and 4000 m, respectively. These characteristics suggest strongly that they were in the dissipating stage.

3.2 Inclusion of microwave-derived LWP into the Z_e analysis

In addition to the LWP derived from (1) (hereafter referred to as LWP_{op}), the LWP can also be obtained using microwave radiation with Advanced Microwave Scanning Radiometer–Earth Observing System (AMSR-E). Hereafter, this microwave-derived LWP is referred to as LWP_{mw}. In general, these two LWPs are different due to their different sensitivities to particle sizes. Their difference could be used to infer information about vertical stratification of cloud particles as argued by Masunaga et al. [39]. The vertical profile of cloud droplet size is known to be variable, and depends on the stage of cloud development. For example, the upper part of non-precipitating clouds contains mainly larger droplets, which grow due to upward motion, with smaller droplets in the lower part. On the contrary, in precipitating clouds, coalesced larger droplets and/or drizzle usually fall to the lower level because of gravity and relatively

smaller droplets remain in the upper part. In their early stages, some drizzling clouds have large drops only near the cloud top, and they are unlikely to contain considerable amounts of water. These differences in characteristics of cloud development stages lead to differences between LWP_{op} and LWP_{mw}. Although LWP_{op} tends to be derived from only smaller cloud droplets (up to 40 μm) that can be retrieved from the visible and near-infrared channels, LWP_{mw} also contains larger droplets, such as drizzle. Thus, LWP_{mw} tends to be larger than LWP_{op} when the cloud is in the mature stage and contains drizzle or precipitation drops, whereas LWP_{mw} tends to be smaller than LWP_{op} when the cloud is at incipient, non-precipitating development stage. The fact that cloud droplet size retrieved from the visible and near-infrared channels is close to that (usually larger) around the cloud top may cause overestimation of LWP for non-precipitating clouds. This difference is well described when the columnar effective radius is introduced and contrasted against the cloud-top effective radius, as proposed by Masunaga et al. [39]. In this study, the columnar effective radius, derived from LWP_{mw} and denoted by r_{e_mw}, was calculated from the following formula, by substituting LWP_{mw} for LWP_{op} in (1):

$$r_{e\_mw}=9\ LWP_{mw} / 5\tau. \qquad (2)$$

Based on this concept, Masunaga et al. [39] produced a diagram with the cloud-top effective radius r_e as the horizontal axis, and the ratio of r_{e_mw} to r_e (hereafter referred to as ratio) as the vertical axis to classify clouds as precipitating or non-precipitating. Using the diagram (figure 5 of Masunaga et al. [39]), referred to as the r_{e_mw} ratio

diagram here, the following interpretations can be made: (1) precipitating for r_e > 15 μm and a ratio > 1, (2) probably drizzling only near the cloud top for r_e > 15 μm and a ratio < 1, (3) non-precipitating for r_e < 15 μm and a ratio < 1, and (4) no convincing interpretation for r_e < 15 μm and a ratio > 1. Possible candidates for (4) are low precipitating clouds overlaid by non-precipitating mid-level clouds [40], air mass entrainment near the cloud top which leads to smaller particle size, and the random error that produces data samples in this domain. Because microwave retrievals are currently available only over water due to the difficulty in treating land surface emissivity, only the Pacific was examined. Figure 11 shows the r_{e_mw} ratio diagram for the Pacific. We observed two main groups: one with a high ratio (5–40) with moderately large r_e values (18–24 μm), and the other with a ratio around unity with a wide range of r_e values (11–38 μm). Using the threshold values of 15 μm for r_e and unity for the ratio, the upper-right, lower-right, and lower-left portions of the r_{e_mw} ratio diagram correspond to precipitation, probably drizzling, and non-precipitating conditions, respectively [39]. Together with the above classification, the following four subgroups denoted by numbered circles in Figure 11 were defined. Subgroups 1, 2, and 3 were characterized by moderately large r_e values (20–25 μm) with different ratio values from approximately 10 (subgroup 1) to 0.6 (subgroup 3), which were classified as drizzling and/or precipitating. In contrast, subgroup 4 had smaller r_e values (10–15 μm) and ratios (< 1), and was classified as non-precipitating.

Figure 12 shows the maxZ_e distributions for the four subgroups. For the drizzling/precipitating clouds of subgroups 1 to 3, the shape of the distribution became

sharper and the mode maxZ_e value increased as the ratio increased. Furthermore, D_{cld} distributions of the four subgroups in Figure 13 clearly correspond to the maxZ_e distributions, which is consistent with Figures 7 (a) and (b) presenting the maxZ_e distribution for D_{cld} categories. This confirms that D_{cld} provides useful information regarding the occurrence of precipitation.

Subgroup 1 had a high LWP (mostly 350–500 g/m^2), estimated from microwaves with moderately large r_e values (20–24 μm) and low optical depth (<6). From the information, it was clear that most cloud water was composed of much larger drops (e.g., drizzle or precipitation drops) than cloud droplets.

In addition, it is worthwhile to note that r_e values retrieved from 2.15-μm were somewhat larger than those retrieved from 3.75-μm, which was used by Masunaga et al. [39], because of the lower absorption at 2.15-μm [21]. The r_e values used in this study were retrieved from the 2.15-μm channel of the MODIS instrument from the CloudSat 2B-TAU product, thus the threshold of 15 μm might be smaller by a few micrometers, if we attempt to interpret the cloud situation using the method proposed by Masunaga et al. [39].

3.3 Relative positioning of the occurrence of precipitation inside clouds

The PDFs of maxZ_e were fully examined over the target areas in terms of several cloud parameters, such as r_e, LWP, and D_{cld}, in the previous subsection. A significant advantage of CPR is that vertical information regarding the physical condition inside clouds can be observed, whereas conventional passive instruments are unable to make

such measurements.

It is of interest to determine where precipitation occurs inside the clouds and how it changes in terms of the variation of the parameters concerned. For this purpose, the probability of precipitation (POP) [22, 24] was adopted as an indicator in this task. In this study, POP in a cloud layer is defined as the ratio of the sample number of Z_e values > 0dBZ to the total sample number in the cloud layer concerned.

To determine the relative position inside clouds, vertical normalization was undertaken such that the cloud top is 0 and the cloud base is 1. Each 240-m-thick cloud layer was assigned to 10 sublayers between the cloud top (0) and the cloud base (1). For example, for two-layer cloud, the first and second layers were assigned from 0 to 0.5 and from 0.6 to 1, respectively. For four-layer cloud, the first, second, third, and fourth layers were assigned from 0 to 0.25, 0.25 to 0.5, 0.5 to 0.75, and 0.75 to 1, respectively. After assigning a cloud layer into 10 sublayers, the POP was calculated for each layer. This procedure was conducted for the three categories of all parameters.

Figures 14(a) and (b) show the vertical profiles of the POP for the scaled cloud layer according to the three categories of r_e. The horizontal axis is the POP; that is, the probability of precipitation (more than 0 dBZ) and the vertical axis is the relative position from the cloud top, taking 0 and 1 at the cloud top and the cloud base, respectively.

Figure 14 (a) shows the Pacific, where the smaller the particle size, the lower the frequency. This is consistent with the discussion in this study. From the cloud top to the cloud center, the POP generally increased, suggesting the onset of more

drizzle/precipitation. The POP then decreased from the cloud center to the cloud base. This behavior can be understood as follows. Near the top of the cloud, droplets became larger through collisional growth and gradually fell due to gravity, with the POP reaching a maximum around the cloud center. Droplet growth still occurred, and consequently particle size increased in the lower part of the cloud, but due to the attenuation of radar reflectivity due to the presence of larger droplets, the POP became smaller toward the cloud base. This tendency of a 'bow' shape was found for each category, with the lrg category being the most remarkable. This is probably because larger particles have a greater influence on both collisional growth and the attenuation effect. The above process is our speculation. Figure 15 would, however, aid its understanding, which is the same as Figure 14 (a) except for the r_e ranges of less than 12 μm and between 13 and 15 μm. In addition to the general features described so far, such as the bow shape and larger frequency in the larger r_e range, the maximum frequency occurs in the upper part (above 0.4) for the smaller r_e range (less than 12 μm) and in the lower part (below 0.4) for the larger r_e range (between 13 and 15 μm) as indicated by circles. This difference is circumstantial evidence of the existence of larger particles in the lower part of the cloud layer due to gravitational settling.

For China in Figure 14 (b), whereas the 'sml' curve showed a gradual increase from the cloud top to the cloud base, the 'lrg' curve exhibited a roughly opposite curve, being almost constant from the cloud top to the cloud center then decreasing to the cloud base. These two curves form a so-called 'funnel' shape. In addition, the 'mid' curve had an shape intermediate between the 'sml' and 'lrg' curves. The mechanism that forms this

1 ‘funnel’ shape could be as follows. Even in the lrg category, collisional growth and
2 gravitational settling of larger particles were less effective compared with the Pacific
3 case. Thus, the POP was almost constant in the cloud center, and then decreased due to
4 the attenuation of radar reflectivity by large particles in the lower part to the cloud base.
5 In the mid category, the POP profile was largely insensitive, but a small decrease was
6 apparent near the cloud base, suggesting the attenuation of radar reflectivity. Finally, in
7 the sml category, collisional growth was not very effective for small particles in the
8 upper part of the cloud; therefore, the POP was almost constant until near the cloud
9 center. However, cloud droplets grew because more coalescence occurred in the lower
10 part of the cloud compared to the upper part, consequently POP took the larger value in
11 the lower part than the upper part. In this case, the lower number of sufficiently large
12 droplets resulted in lack of attenuation in the radar reflectivity. In China, this process of
13 droplet growth in the lower part of the cloud was similar to that in the upper part of the
14 cloud in the Pacific, as shown in Figure 14 (a). To investigate this situation more
15 thoroughly, the sml category (less than 14 μm) was divided into two ranges of less than
16 10 μm (sml1) and between 10 and 12 μm (sml2). Figure 16 shows the POP profile
17 inside the clouds over China for the sml1 and sml2 categories. The rapid increase in the
18 POP was more marked from near the cloud center toward the cloud base for r_e values <
19 10 μm. This suggests that particle growth could become very efficient in the lower part
20 of the cloud even when cloud-top droplets are small. Moreover, a generally gradual
21 increase in the POP was observed throughout the cloud layer, with the exception of a
22 small decrease just below the cloud center for the sml2 category.

4 Conclusions

This paper studied the behavior of 94-GHz radar reflectivity with variation in the properties of low-level water clouds, such as the effective droplet radius (r_e), cloud depth (D_{cld}), and liquid water path (LWP), over the northwest Pacific and China at mid-latitudes to better understand the transition processes among cloud droplets, drizzle, and precipitation over these areas.

Before entering the main body of the analyses, several characteristics of the probability density functions (PDFs) of the cloud parameters were described. Overall, the parameters were larger over the Pacific Ocean than over China. The three following analyses were carried out.

First, the cloud parameters were divided into three categories: the small (sml), middle (mid), and large (lrg) bins. Then, changes in the distribution of maxZ_e were examined in terms of variation in the cloud parameters. Regarding variation in r_e and D_{cld}, maxZ_e had monomodal distributions, and each modal value increased as the category shifted to larger values. Rosenfeld and Gutman [41] and Rosenfeld [42] noted that cloud particle size contains sufficient information on the onset of precipitation. The above findings also mean that D_{cld} contains considerable information on the onset of precipitation. Moreover, regarding variation in LWP_{op}, note that the distribution of maxZ_e in the sml category was bimodal, with peaks around –20 and 15 dBZ, unlike the mid and lrg categories, which had monomodal distributions. Examinations of the distribution of r_e in each LWP category and that of maxZ_e in each r_e category for the sml

category of LWP confirmed that the sml category of LWP contained two different types of cloud: non-precipitating clouds in the incipient stage characterized by smaller r_e values and raining clouds in their dissipating stage characterized by larger r_e values.

Second, LWP_{mw}, which was obtained only over ocean, was analyzed together with LWP_{op} using a diagram proposed by Masunaga et al. [39]. This diagram, referred to as the r_{e_mw} ratio diagram in this study, classifies three types of precipitation, *i.e.* precipitating, probably drizzling only near the cloud top, and non-precipitating, according to threshold values of r_e near the cloud top and the ratio of the column effective radius to the cloud-top effective radius. Plotting data on the r_{e_mw} ratio diagram produced two main groups for the Pacific case. One had a high ratio with moderately large r_e in which cloud water comprised mostly much larger drops. The other had a ratio around unity with a wide range of r_e that could be classified into three precipitation types using the above criteria. Incorporating maxZ_e and D_{cld}, which were determined from the CPR radar reflectivity, into the r_{e_mw} ratio diagram corroborated the usefulness of this analysis method and the importance of D_{cld} for examining the occurrence of precipitation.

Third, the vertical profile of maxZ_e, *i.e.*, the position of maxZ_e relative to the cloud top, was investigated using a measure of the probability of precipitation (POP) according to variation in r_e. This analysis takes advantage of the radar profile information inside the cloud layer. The results showed that the Pacific and China cases had ‘bow’ and ‘funnel’ shapes, respectively. The emergence of vertical POP profiles that assumed these shapes according to the variation in r_e was interpreted as the

enhancement of Z_e due to droplet collisional growth and the attenuation of Z_e by the presence of large particles. Furthermore, a detailed analysis of smaller particles (<10 μm) reinforced the idea of rapid, efficient particle growth in the lower part of the cloud.

Finally, a necessary future direction is discussed briefly. Despite the importance of the aerosol indirect effect in the climate system, as stated earlier, this study does not address it explicitly. The effects of aerosols on the Z_e distribution and the vertical profile of POP should be analyzed and revealed observationally, although it would be very difficult to isolate only the effects of aerosols [43]. As this study depended entirely on observational data, the qualitative features derived in this study should be made more quantitative by using numerical models. This approach will greatly facilitate our understanding of the currently unknown cloud–precipitation transition processes. In addition to the regional analysis performed in this study, global-scale analysis is required to establish a more complete picture of the relationships between Z_e and cloud parameters.

Acknowledgments

K. Kawamoto is supported by Grant-in aid for Scientific Research (B), Grant-in aid for Challenging Exploratory Research and Grant-in aid for Scientific Research on Innovative Areas. The CloudSat data products of 2B-GEOPROF, 2B-TAU, 2C-PRECIP-COLUMN and ECMWF-AUX were provided by the CloudSat Data

Processing Center at CIRA/Colorado State University. Part of this research was carried out at the Jet Propulsion Laboratory, California Institute of Technology, under a contract with the National Aeronautics and Space Administration.

References

[1] Stephens GL, et al. The CloudSat mission and the A-Train. Bull Am Meteorol Soc 2002;83:1771–90.

[2] Twomey S. The influence of pollution on the shortwave albedo of clouds. J Atmos Sci 1977;34:1149–52.

[3] Albrecht B. Aerosols, cloud microphysics, and fractional cloudiness. Science 1989;245:1227–30.

[4] Platnick S, King MD, Ackerman SA, Menzel WP, Baum BA, Riedi JC, Frey RA, The MODIS cloud products: Algorithms and examples from Terra. IEEE Trans. Geosci. Remote Sens 2003;41:459–73.

[5] Koren I, Kaufman YJ, Rosenfeld D, Remer LA, Rudich Y. Aerosol invigoration and restructuring of Atlantic convective clouds. Geophys Res Lett 2005;32:L14828.

[6] Suzuki K, Nakajima T, Numaguti A, Takemura T, Kawamoto K, Higurashi A. A study of the aerosol effect on a cloud field with simultaneous use of GCM modeling and satellite observation. J Atmos Sci 2004;61:179–94.

[7] Quaas J, Min Y, Menon S, Takemura T, Wang M, Penner JE, et al. Aerosol indirect effects - general circulation model intercomparison and evaluation with satellite data. Atmos Chem Phys 2009;9:8697–717.

[8] Randall DA, Coakley JA, Fairall CW, Kropfli, RA, Lenschow, DH. Outlook for research on subtropical marine stratiform clouds. B Am Meteor Soc 1984;65:1290–1301.

[9] IPCC. Climate Change, The Physical Science Basis. Stocker TF, Qin D, Plattner GK, Tignor M, Allen SK, Boschung J, et al. (eds.). Cambridge University Press: Cambridge and New York;2013.

[10] Han Q, Rossow WB, Lacis AA. Near-global survey of effective droplet radii in liquid water clouds using ISCCP data. J Clim 1994;7:465–97.

[11] Nakajima TY, Nakajima T. Wide-area determination of cloud microphysical properties from NOAA AVHRR measurements for FIRE and ASTEX regions. J Atmos Sci 1995;52:4043–59.

[12] Kawamoto K, Nakajima T, Nakajima TY. A global determination of cloud microphysics with AVHRR remote sensing. J Clim 2001;14: 2054–68.

[13] Higurashi, A, Nakajima T. Development of a two channel aerosol retrieval algorithm on a global scale using NOAA/ AVHRR. J Atmos Sci 1999;56:924–41.

[14] Nakajima T, Higurashi A, Kawamoto K, Penner JE. A possible correlation between satellite-derived cloud and aerosol microphysical parameters. Geophys Res Lett 2001;28:1171–74.

[15] Bréon FM, Tanré D, Generoso S. Aerosols effect on cloud droplet size monitored from satellite. Science 2002;295:834–38.

[16] Lin B, Rossow WB. Observations of cloud liquid water path over oceans: Optical and microwave remote sensing methods. J Geophys Res 1994;99:20907-27.

[17] Lin B, Rossow WB. Seasonal variation of liquid and ice water path in non-precipitating clouds over oceans. J Clim 1996;9:2890-902.

[18] Lin B, Minnis P, Wielicki BA, Doelling DR, Palikonda, R, Young DF, et al. Estimation of water cloud properties from satellite microwave and optical measurements in oceanic environments. II: Results. J Geophys Res 1998;103:3887-905.

[19] Ho S, Lin B, Minnis P, Fan TF. Estimation of cloud vertical structure and water amount over tropical oceans using VIRS and TMI data. J Geophys Res 2003;108 (D14):4419, doi:10.1029/2002JD003298.

[20] Huang J, Minnis P, Lin B, Yi Y, Khaiyer MM, Arduini RF, et al. Advanced retrievals of multilayered cloud properties using multi-spectral measurements. J Geophys Res 2005;110, D15S18:doi:10.1029/2004JD005101.

[21] Nakajima T, King MD. Determination of the optical thickness and effective particle radius of clouds reflected solar radiation measurements. Part I: Theory. J Atmos Sci 1990;47:1878–93.

[22] Lebsock MD, Stephens GL, Kummerow C. Multisensor satellite observations of aerosol effects on warm clouds. J Geophys Res 2008;113:D15205:http://dx.doi.org/10.1029/2008JD009876.

[23] Kubar TL, Hartmann DL, Wood R. Understanding the importance of microphysics and macrophysics for warm rain in marine low clouds. Part I: Satellite observations. J Atmos Sci 2009;66:2953–72.

[24] L'Ecuyer TS, Berg W, Haynes JM, Lebsock MD, Takemura T. Global observations of aerosol impacts on precipitation occurrence in warm maritime clouds. J Geophys Res 2009;114:D09211:http://dx.doi.org/10.1029/2008JD011273.

[25] Kawamoto K, Suzuki K. Microphysical transition in water clouds over the Amazon and China derived from space-borne radar and radiometer data. J Geophys Res 2012;117:D05212:http://dx.doi.org/10.1029/2011JD016412.

[26] Nakajima TY, Suzuki K, Stephens GL. Droplet growth in warm water clouds observed by the A-Train. Part II: a multi-sensor view. J Atmos Sci 2010;67:1897–907.

[27] Suzuki K, Nakajima TY, Stephens GL. Particle growth and drop collection efficiency of warm clouds as inferred from joint CloudSat and MODIS observations. J Atmos Sci 2010;67:3019–32.

[28] Suzuki K, Stephens GL, van den Heever SC, Nakajima TY. Diagnosis of the warm rain process in cloud-resolving models using joint CloudSat and MODIS observations. J Atmos Sci 2011;68:2655–70.

[29] Suzuki K, Stephens GL, Lebsock MD. Aerosol effect on the warm rain formation process: Satellite observations and modeling. J Geophys Res 2013;118:doi:10.1029/2012JD018722.

[30] Kawamoto K, Suzuki K. Comparison of water cloud microphysics over mid-latitude land and ocean using CloudSat and MODIS observations. JQSRT 2013;122:13–24.

[31] Mace GG, Marchand R, Zhang Q, Stephens GL. Global hydrometeor occurrence as observed by CloudSat: initial observations from summer 2006. Geophys Res Lett

2007;34:L09808. http://dx.doi.org/10.1029/2006GL029017.

[32] Marchand R, Mace GG, Ackerman T, Stephens GL. Hydrometeor detection using CloudSat—An Earth-orbiting 94 GHz cloud radar. J Atmos Ocean Tech 2008;25:519–33.

[33] Polonsky I. Level 2 cloud optical depth product process description and interface control document. CloudSat Project, CIRA, Colorado State University, Fort Collins;2008:21 pp. Available from /http://www.cloudsat.cira.clostate.edu/ICD/2BTAU/2B-TAU_P DICD_5.0.pdfS.

[34] Haynes J, L'Ecuyer TS, Stephens GL, Miller SD, Mitrescu C, Wood NB, Tanelli S. Rainfall retrieval over the ocean with spaceborne W-band radar. J Geophys Res 2009;114:D00A22, doi:10.1029/2008JD009973.

[35] Partain P. Cloudsat ECMWF-AUX auxiliary data process description and interface control document. CloudSat Project, CIRA. Fort Collins: Colorado State University, Fort Collins; 2007:10 pp. Available from:

/http://www.cloudsat.cira.colostate.edu/dataICDlist.php?go=list&
path=/ECMWF-AUXS.

[36] Stephens GL. Radiation profiles in extended water clouds. Part II: Parameterization schemes. J Atmos Sci 1978;35:2123–32.

[37] Brenguier J, Pawlowska H, Schuller L, Preusker R, Fischer J, Fouquart Y. Radiative properties of boundary layer clouds: droplet effective radius versus number concentration. J Atmos Sci 2000;57:803–21.

[38] Wood R, Drizzle in stratiform boundary layer clouds. Part I: Vertical and horizontal structure. J Atmos Sci 2005;62:3011–33.

[39] Masunaga H, Nakajima TY, Nakajima T, Kachi M, Oki R, Kuroda S. Physical properties of maritime low clouds as retrieved by combined use of Tropical Rainfall Measurement Mission Microwave Imager and Visible/Infrared Scanner: Algorithm. J Geophys Res 2002;107:No.D10, 10.1029/2001JD000743.

[40] Lensky IM, Rosenfeld D. Estimation of precipitation are and rain intensity based on the microphysical properties retrieved from NOAA AVHRR data. J Appl Meteorol 1997;36:234–42.

[41] Rosenfeld D, Gutman G. Retrieving microphysical properties near the tops of potential rain clouds by multispectral analysis of AVHRR data. J Atmos Sci 1994;34:259–83.

[42] Rosenfeld D. Suppression of rain and snow by urban and industrial air pollution. Science 2000;287:1793–96.

[43] Koren I, Feingold G, Remer LA. The invigoration of deep convective clouds over the Atlantic: aerosol effect, meteorology or retrieval artifact? Atmos Chem Phys 2010;10:8855-88.

Table 1 The ranges of all category of each cloud parameter,

parameter	sml	mid	lrg
Effective Particle Radius	smaller than 14μm	14 – 22μm	larger than 22μm
Liquid Water Path	less than 80g/m²	80 – 120g/m²	more than 120g/m²
Cloud Geometrical Thickness	thinner than 500m	500 – 1500m	thicker than 1500m

Figures

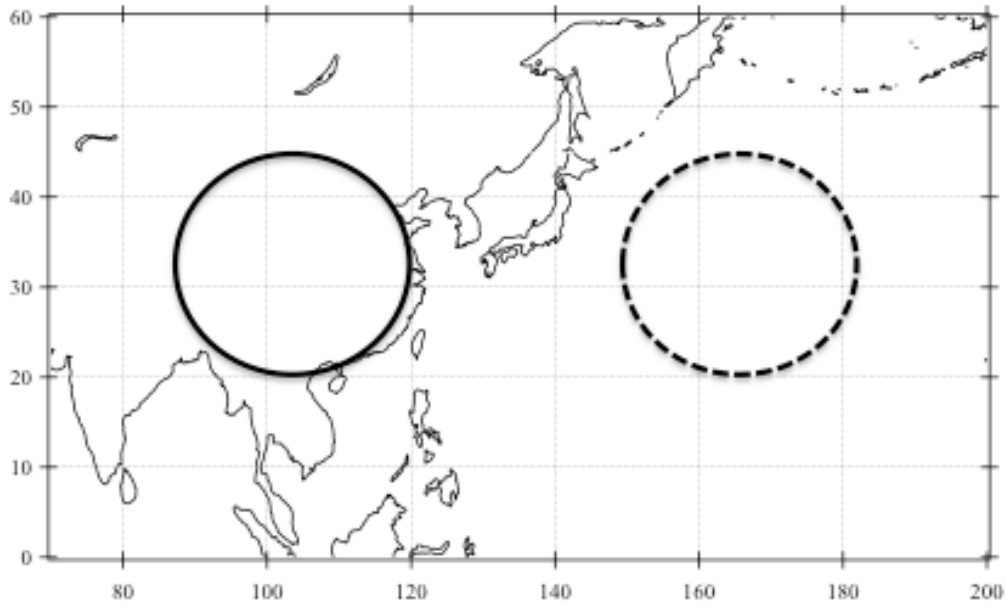

Figure 1

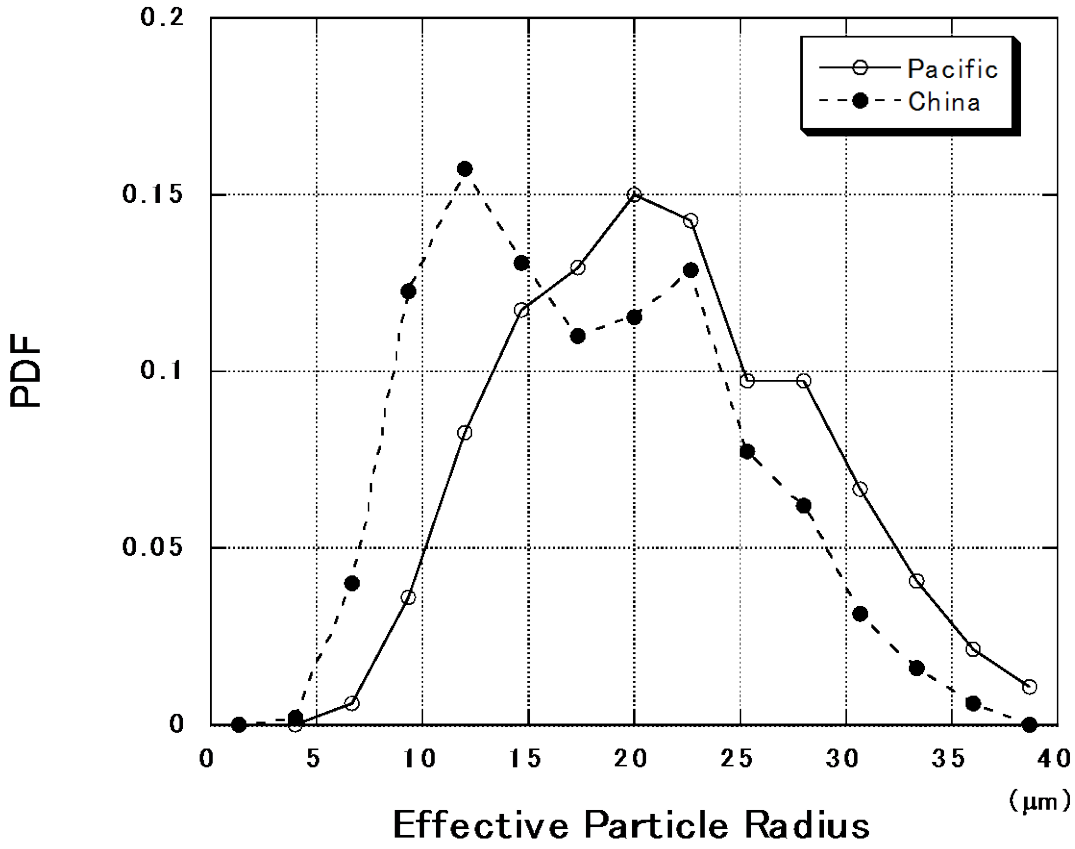
0.2
0.15
0.1
0.05
0
PDF
Pacific
China
0
5
10
15
20
25
30
35
40
(μm)
Effective Particle Radius

Figure 2

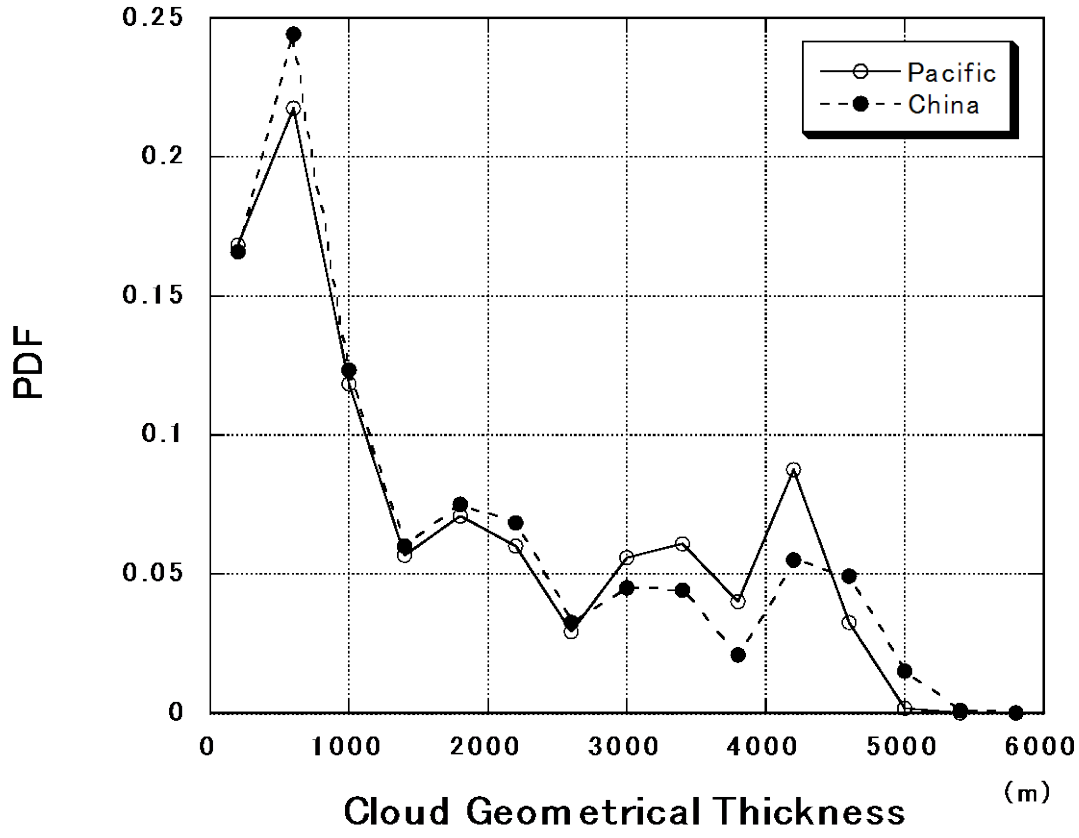
0.25
0.2
0.15
0.1
0.05
0
PDF
Pacific
China
0
1000
2000
3000
4000
5000
6000
(m)
Cloud Geometrical Thickness

1

2 Figure 3

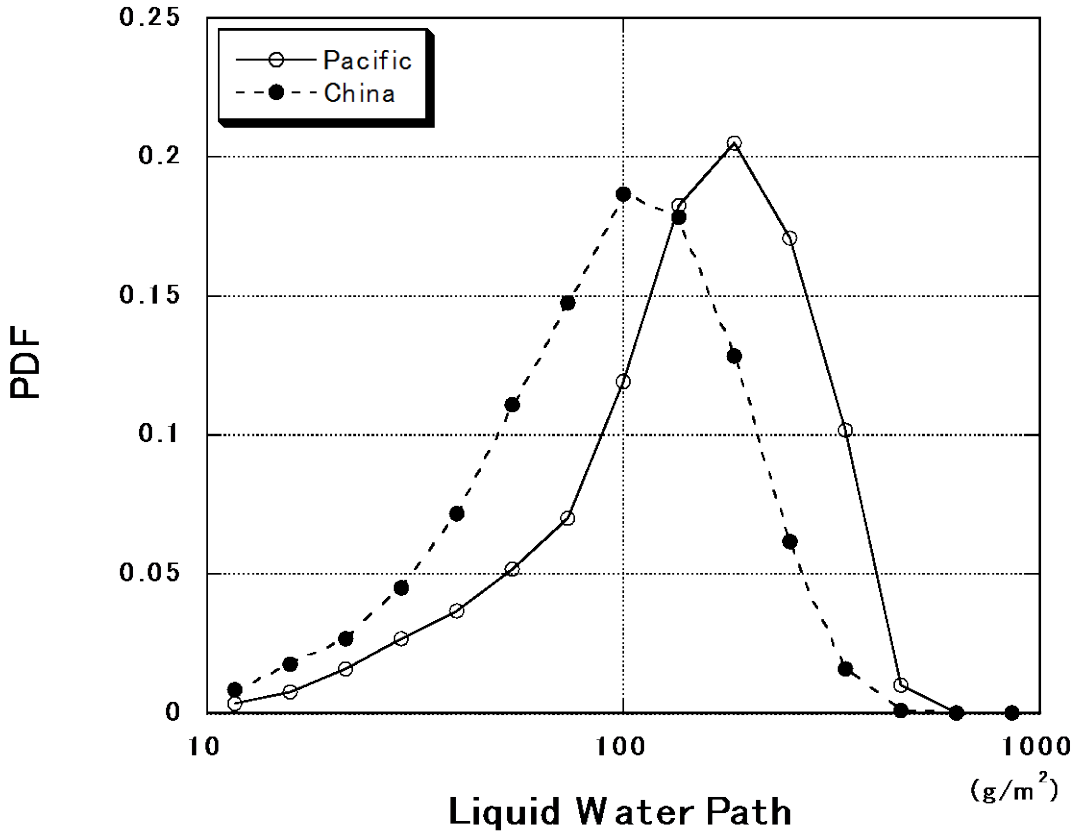
0.25
0.2
0.15
0.1
0.05
0
PDF
Pacific
China
10
100
1000
(g/m²)
Liquid Water Path

1

2 Figure 4

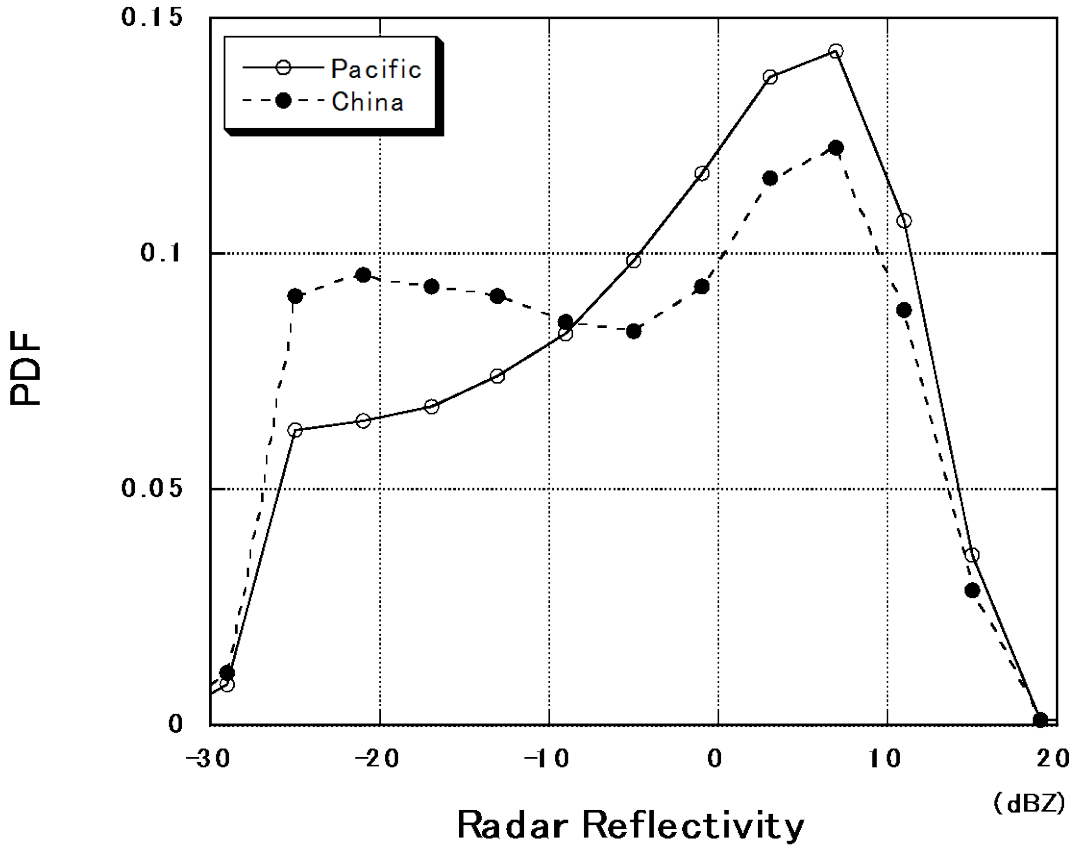
0.15
0.1
0.05
0
PDF
Pacific
China
-30
-20
-10
0
10
20
(dBZ)
Radar Reflectivity

Figure 5

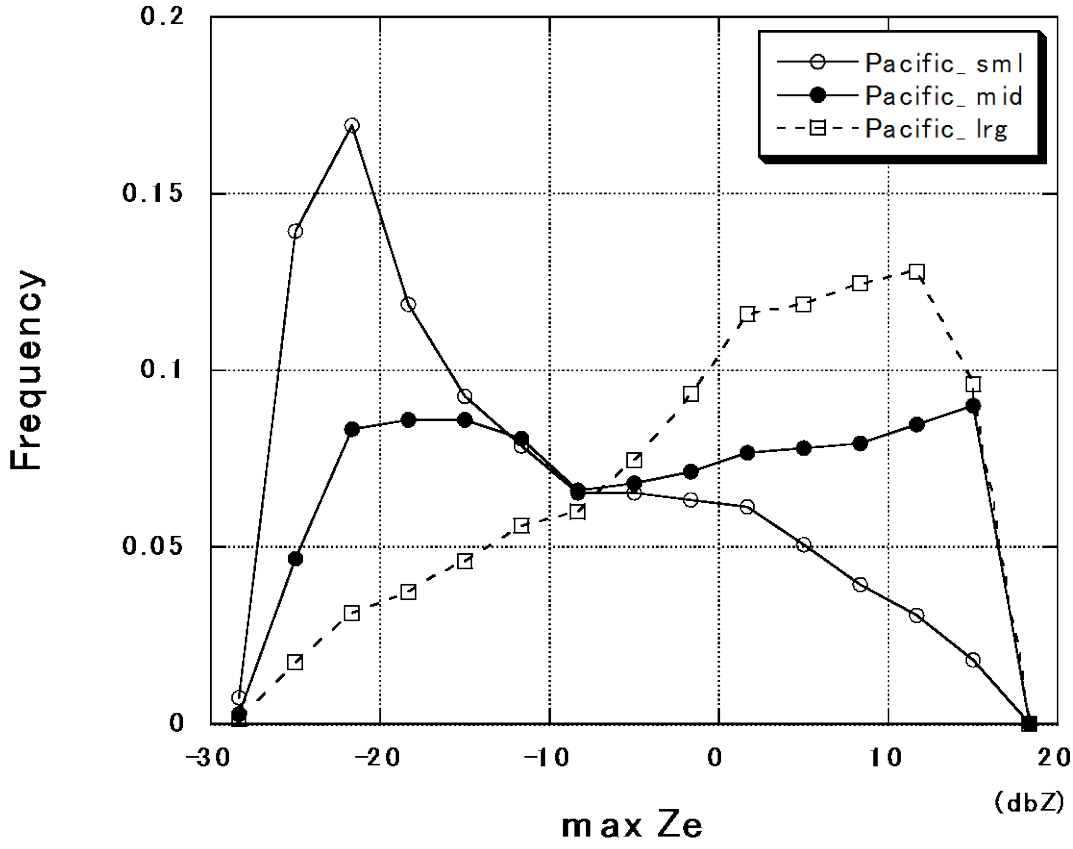
0.2
0.15
0.1
0.05
0
Frequency
Pacific_ sml
Pacific_ mid
Pacific_ lrg
-30
-20
-10
0
10
20
(dbZ)
max Ze

Figure 6 (a)

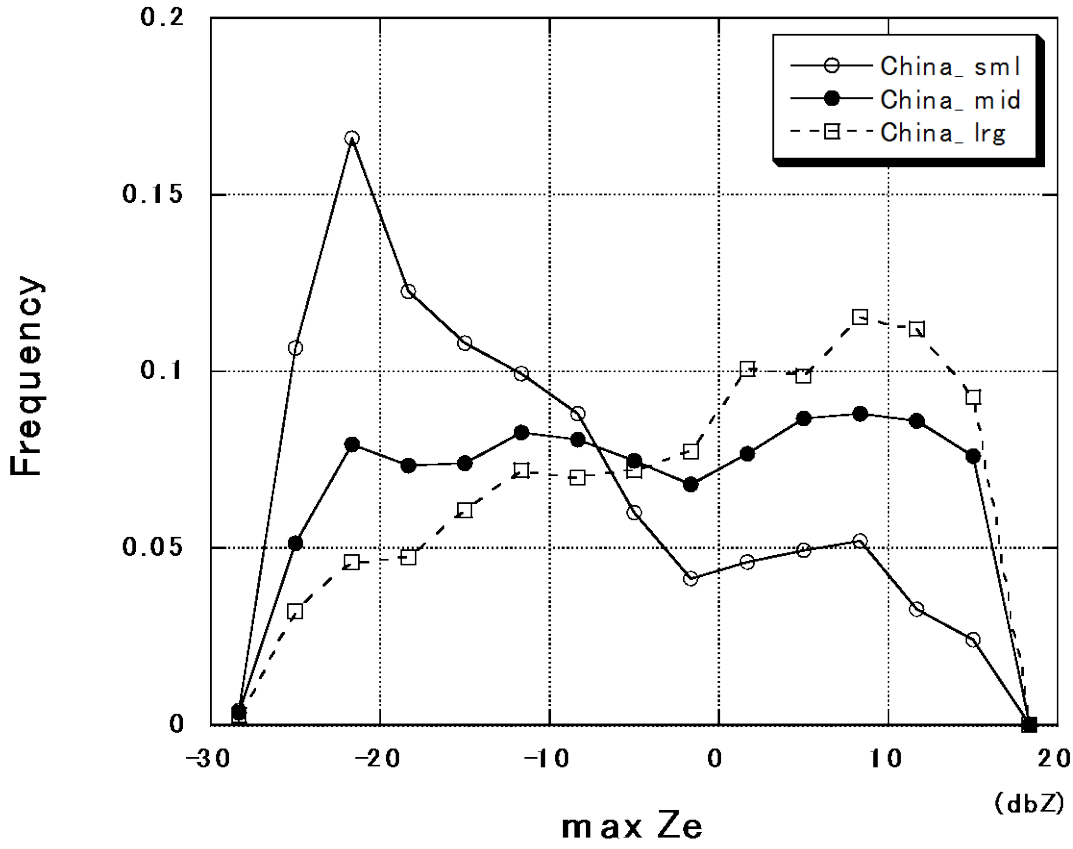
0.2
0.15
0.1
0.05
0
Frequency
China_ sml
China_ mid
China_ lrg
-30
-20
-10
0
10
20
(dbZ)
max Ze

Figure 6 (b)

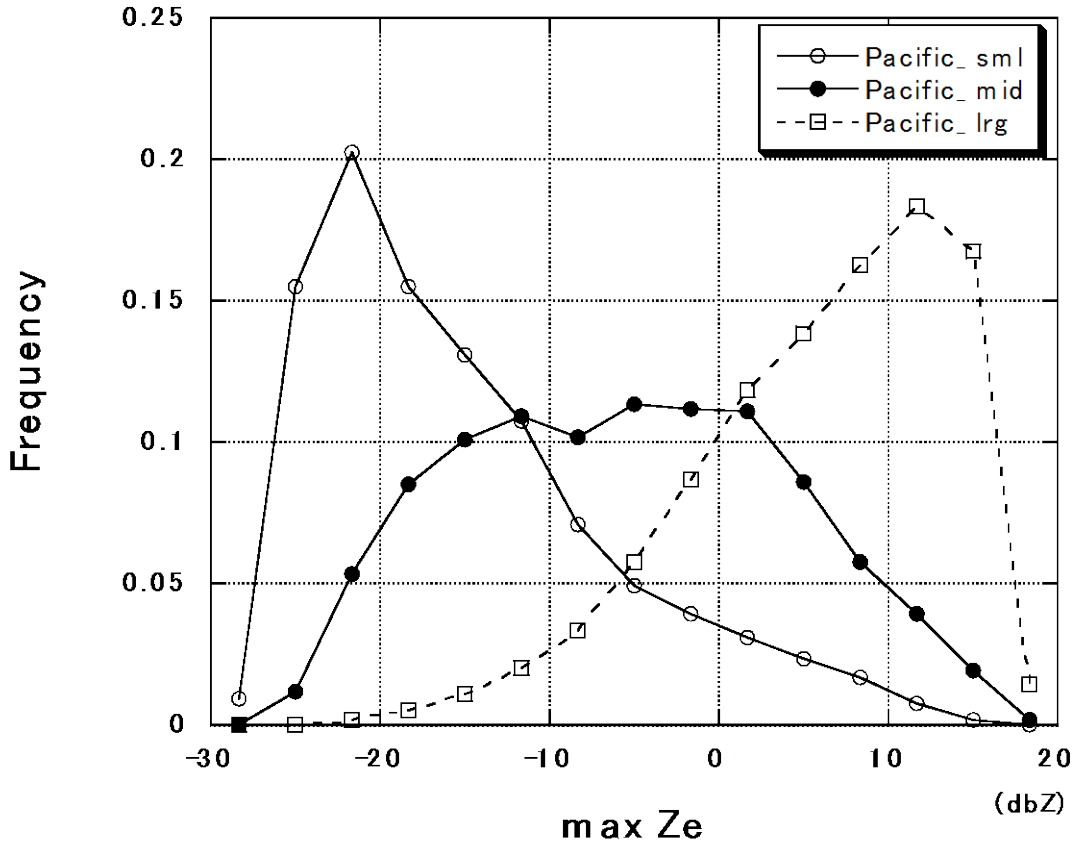
0.25
0.2
0.15
0.1
0.05
0
Frequency
-30
-20
-10
0
10
20
(dbZ)
max Ze
Pacific_ sml
Pacific_ mid
Pacific_ lrg

1

2 Figure 7 (a)

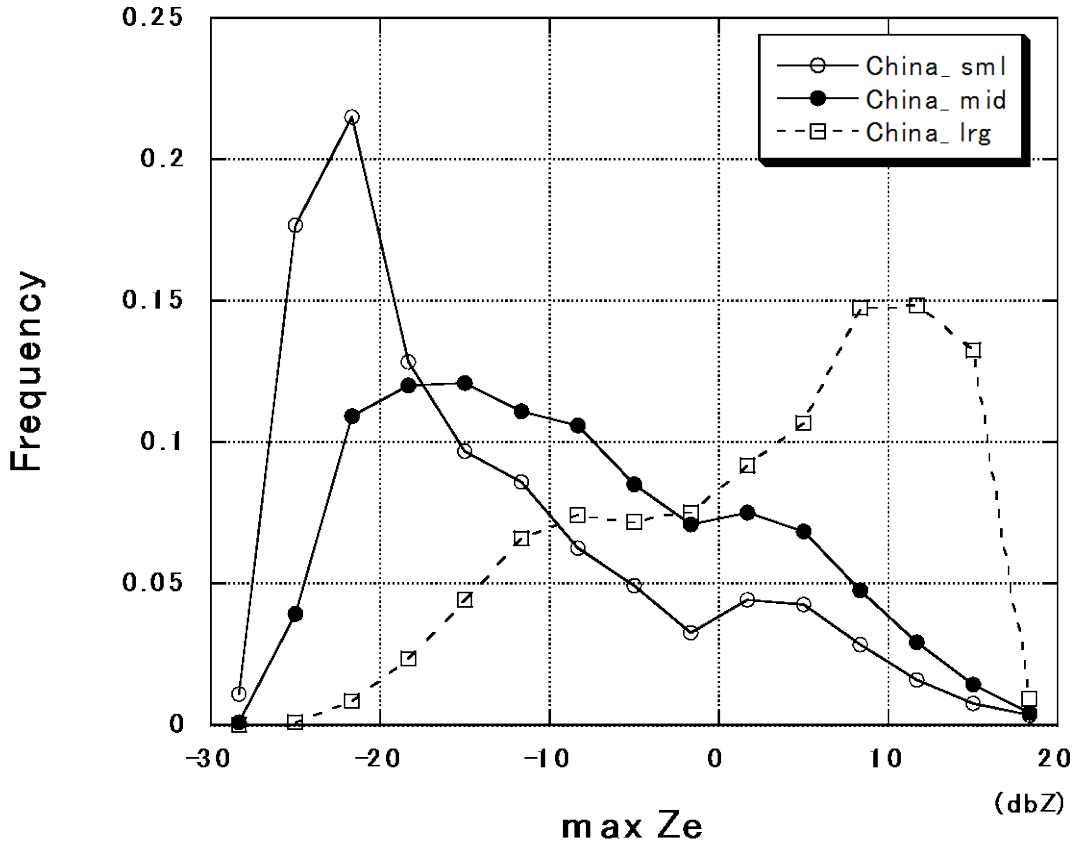
0.25
0.2
0.15
0.1
0.05
0
Frequency
China_ sml
China_ mid
China_ lrg
-30
-20
-10
0
10
20
(dbZ)
max Ze

1

2 Figure 7 (b)

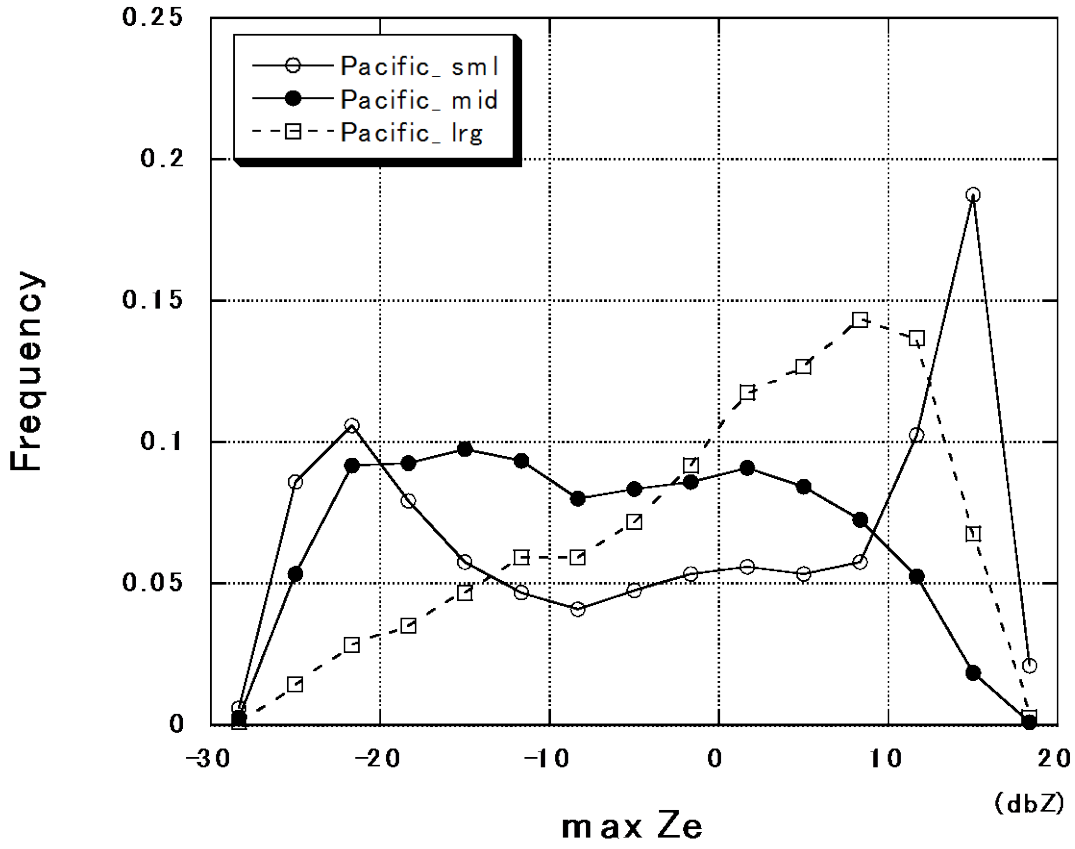
0.25
0.2
0.15
0.1
0.05
0
Frequency
Pacific_ sml
Pacific_ mid
Pacific_ lrg
-30
-20
-10
0
10
20
(dbZ)
max Ze

Figure 8 (a)

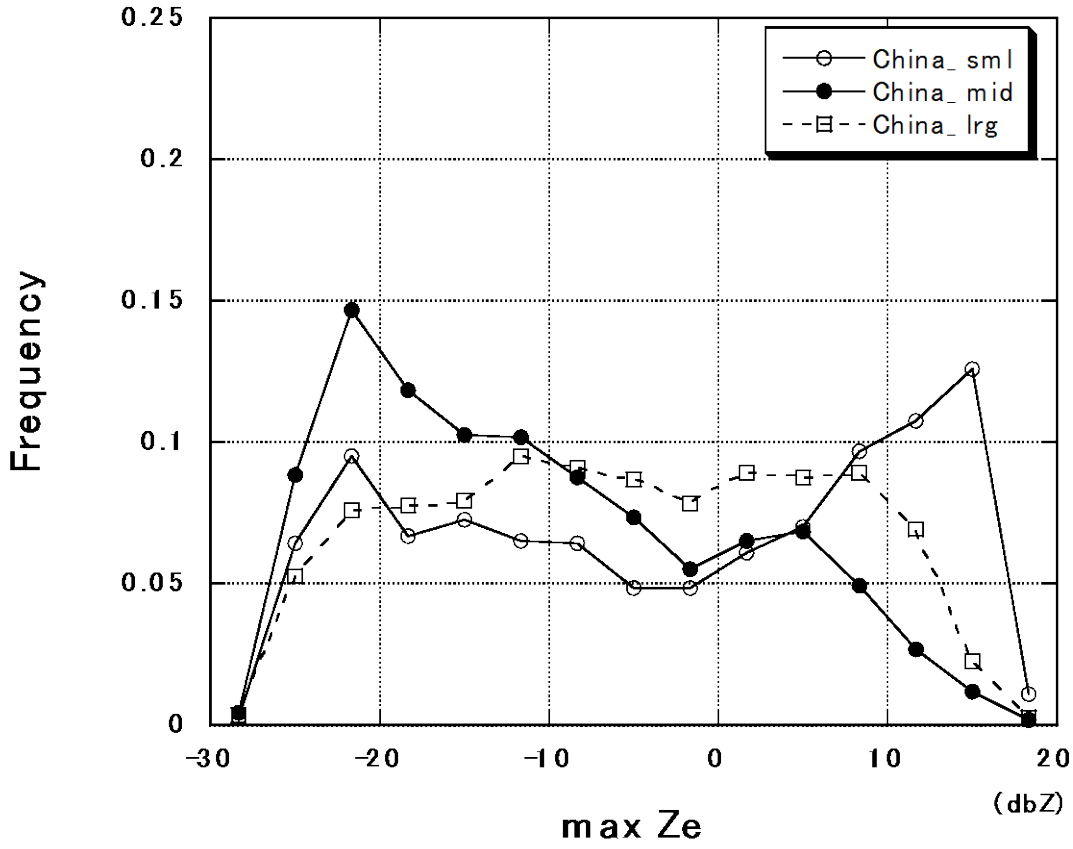
0.25
0.2
0.15
0.1
0.05
0
Frequency
China_ sml
China_ mid
China_ lrg
-30
-20
-10
0
10
20
(dbZ)
max Ze

Figure 8 (b)

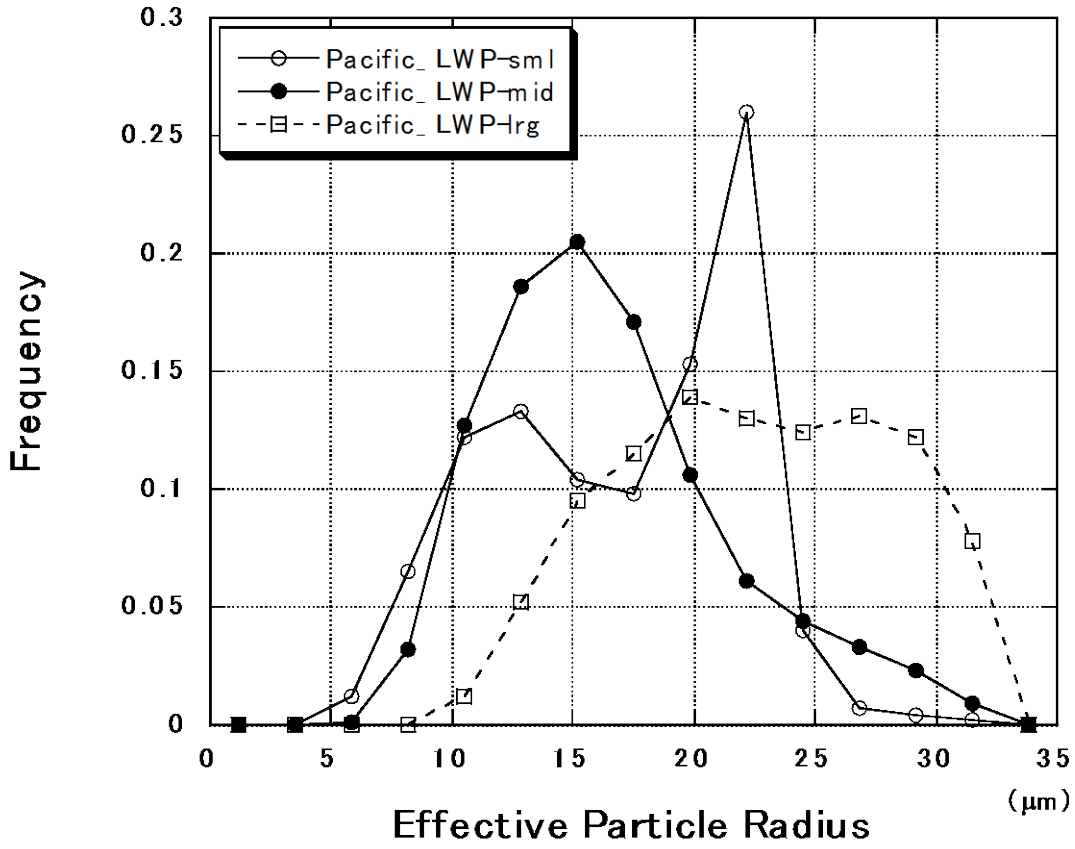
Pacific_ LWP-sml
Pacific_ LWP-mid
Pacific_ LWP-lrg
Frequency
0.3
0.25
0.2
0.15
0.1
0.05
0
0
5
10
15
20
25
30
35
(μm)
Effective Particle Radius

Figure 9 (a)

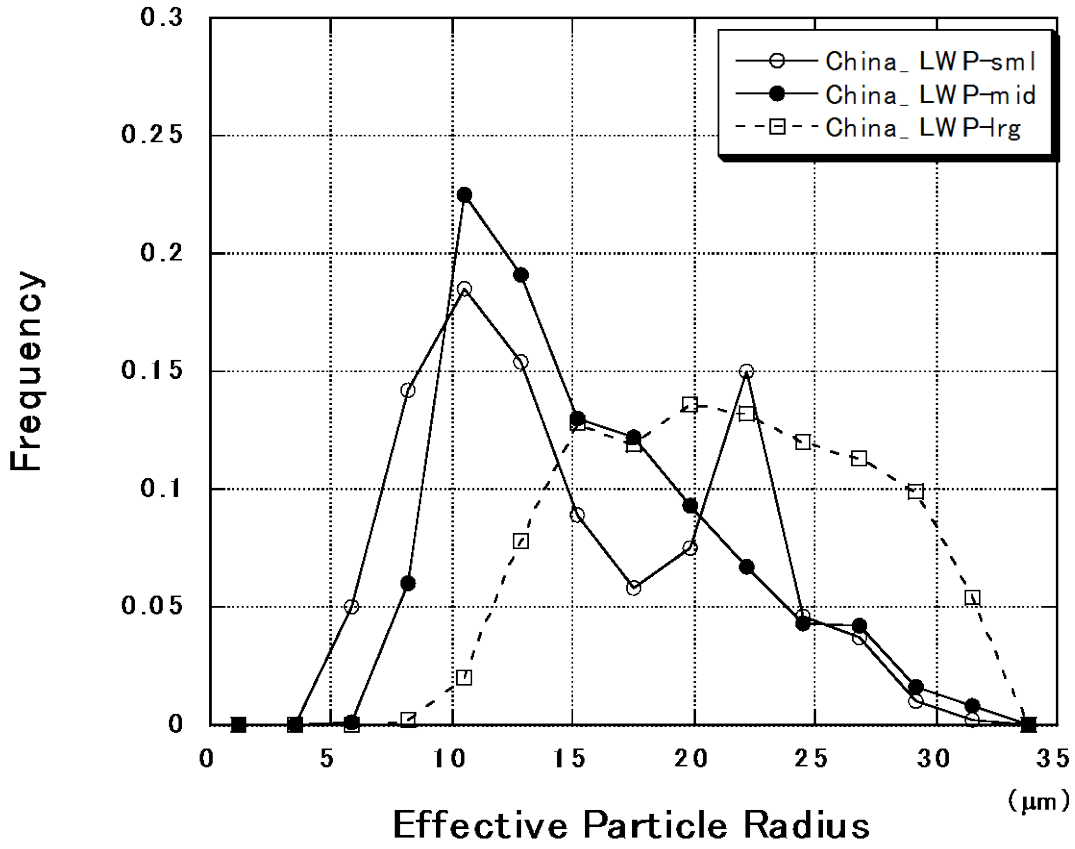
China_ LWP-sml
China_ LWP-mid
China_ LWP-lrg
Frequency
0.3
0.25
0.2
0.15
0.1
0.05
0
0
5
10
15
20
25
30
35
(μm)
Effective Particle Radius

Figure 9 (b)

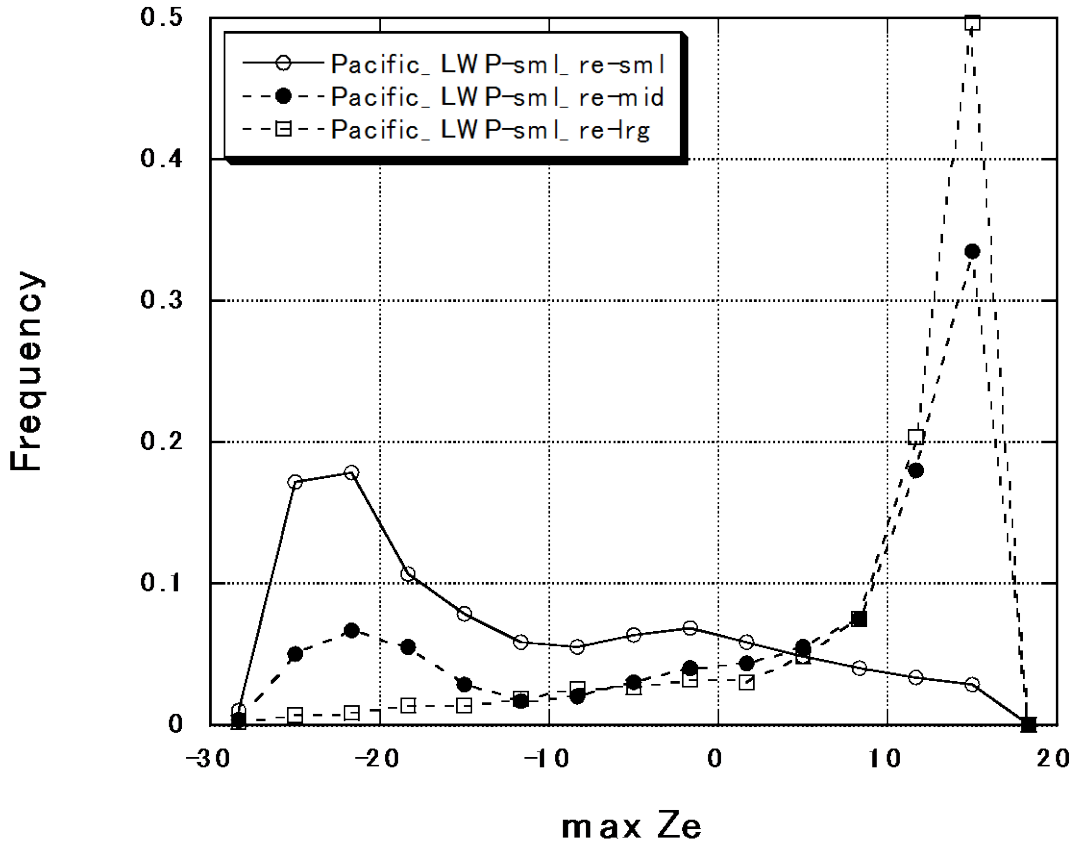
Pacific_LWP-sml_re-sml
Pacific_LWP-sml_re-mid
Pacific_LWP-sml_re-lrg
Frequency
0.5
0.4
0.3
0.2
0.1
0
-30
-20
-10
0
10
20
max Ze

Figure 10 (a)

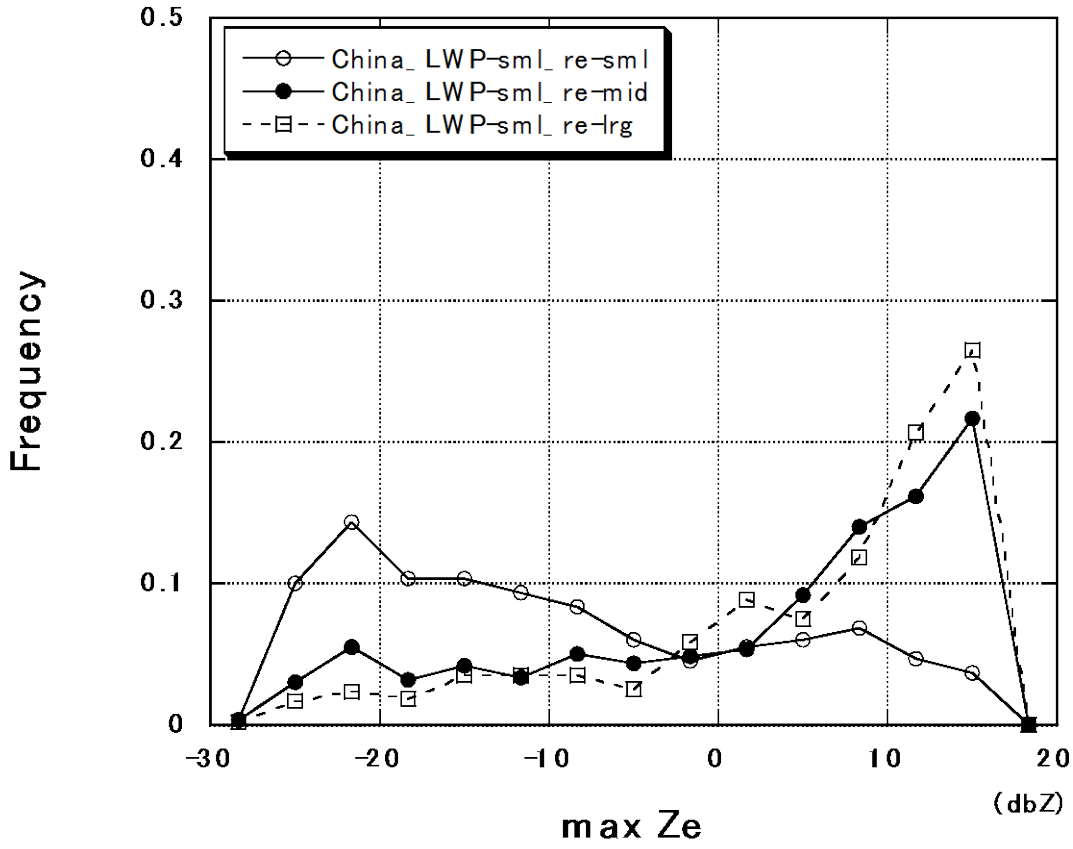

1

2 Figure 10 (b)

3

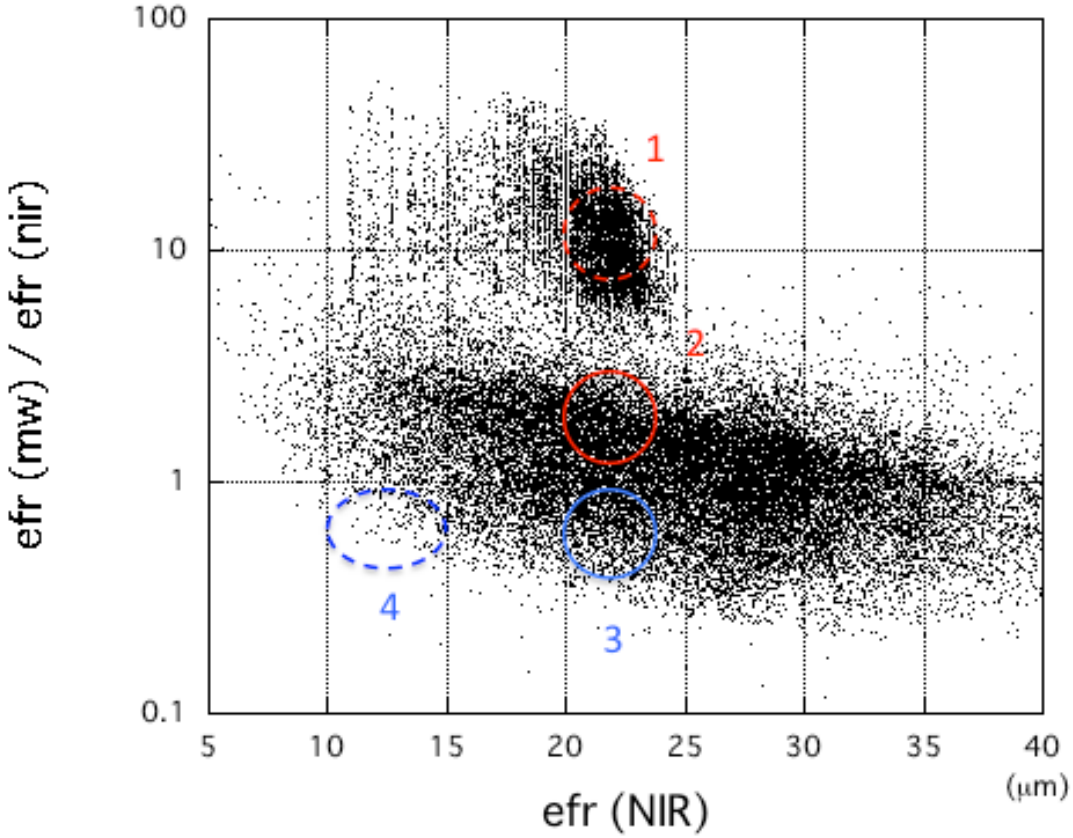

Figure 11

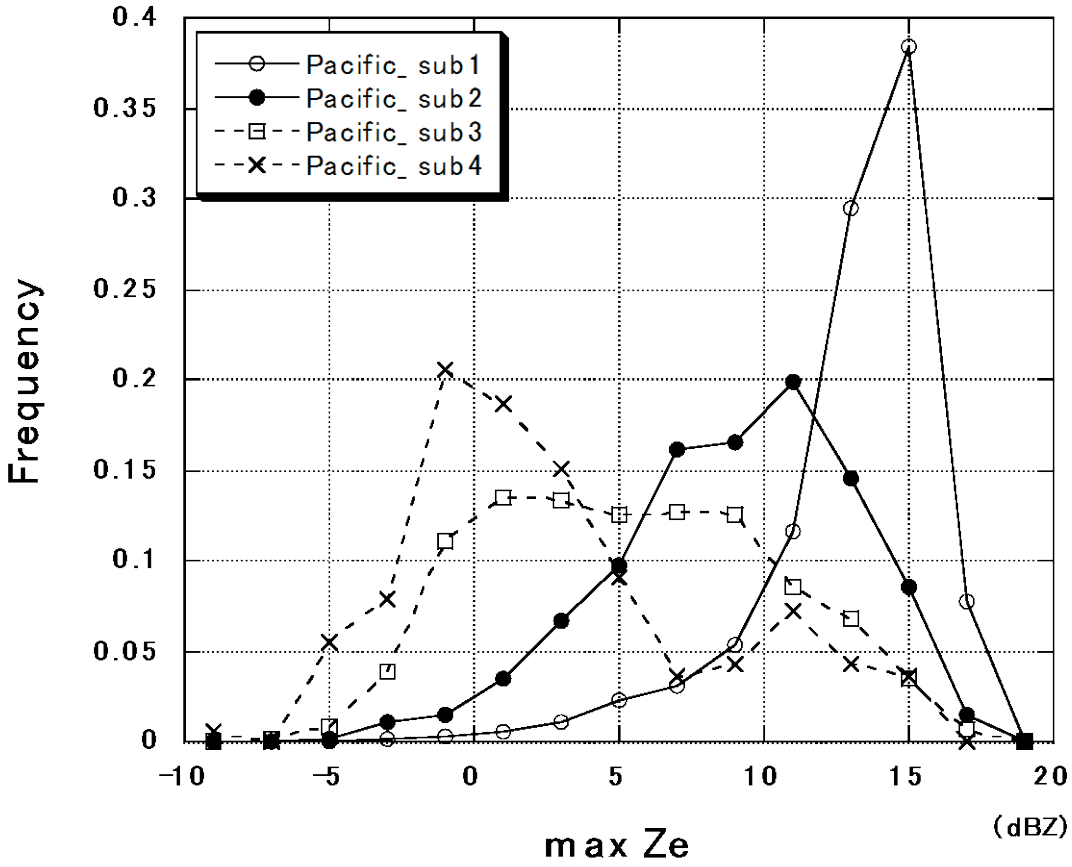
Pacific_ sub1
Pacific_ sub2
Pacific_ sub3
Pacific_ sub4
Frequency
0.4
0.35
0.3
0.25
0.2
0.15
0.1
0.05
0
−10
−5
0
5
10
15
20
max Ze
(dBZ)

1

2 Figure 12

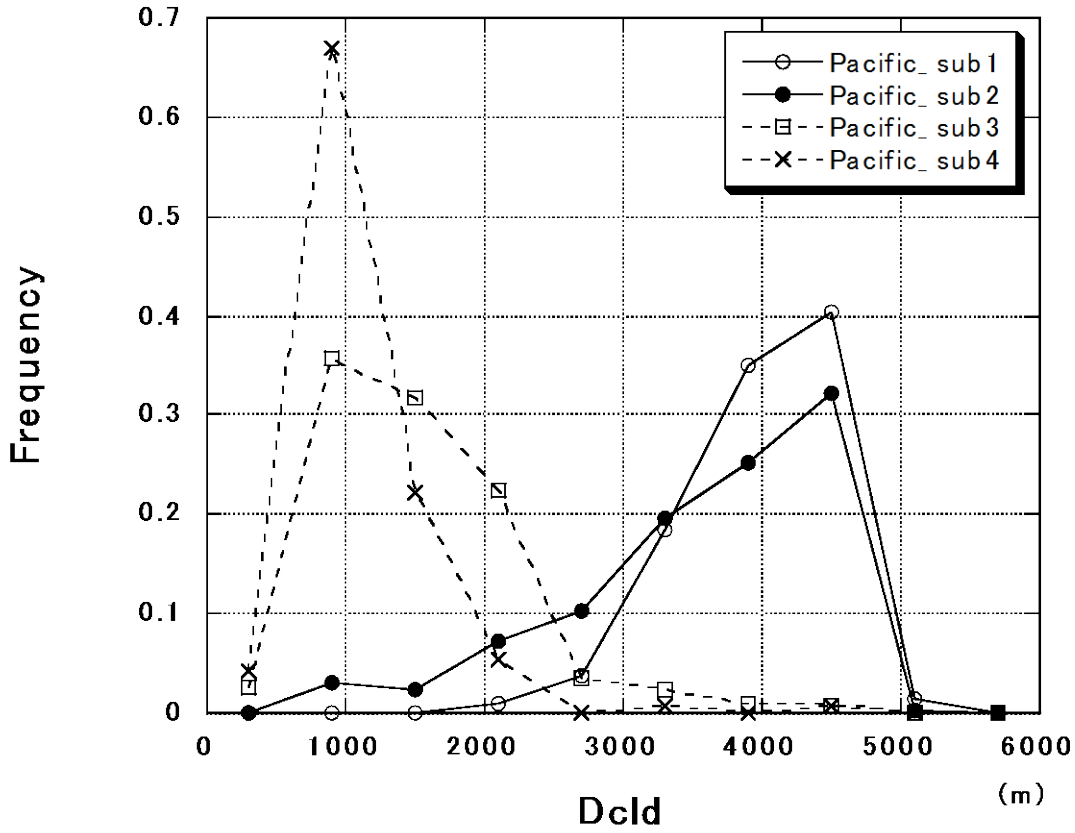

1

2 Figure 13

3

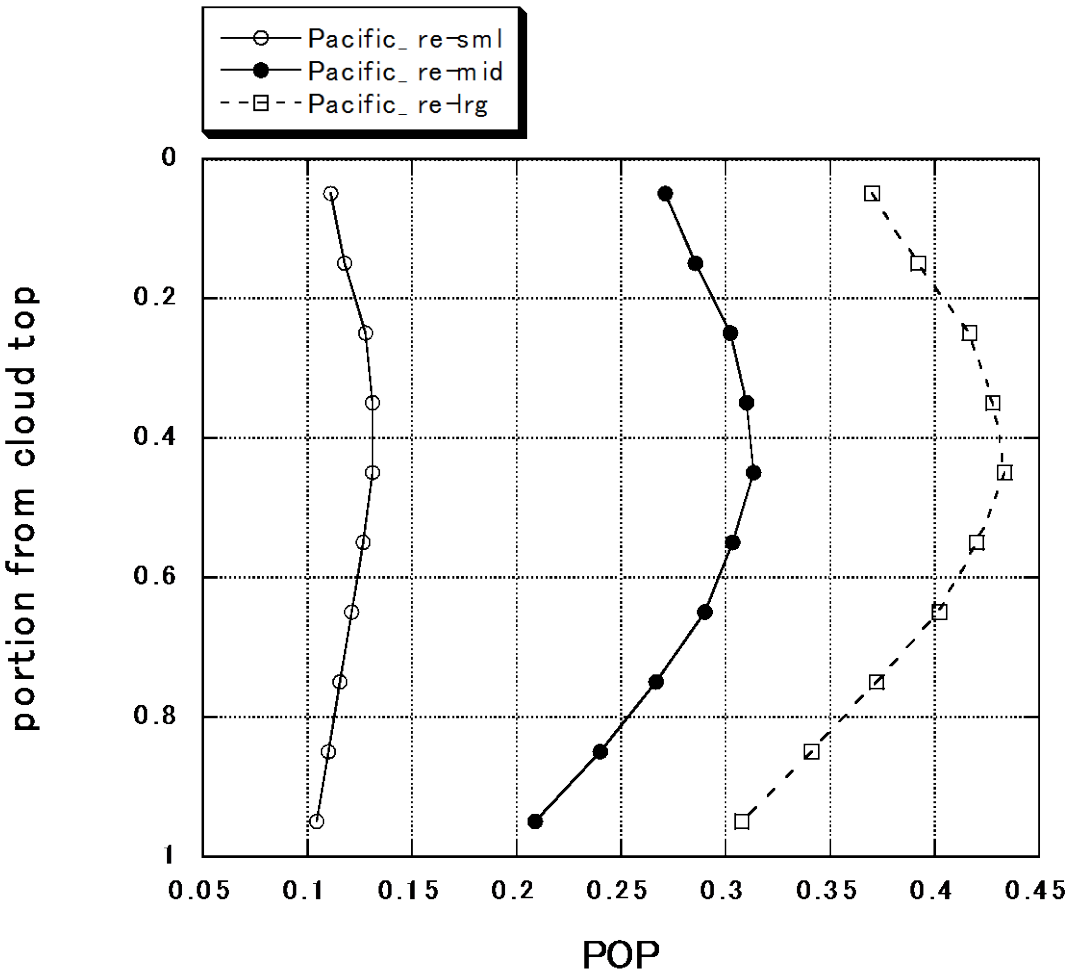

1

2 Figure 14 (a)

3

4

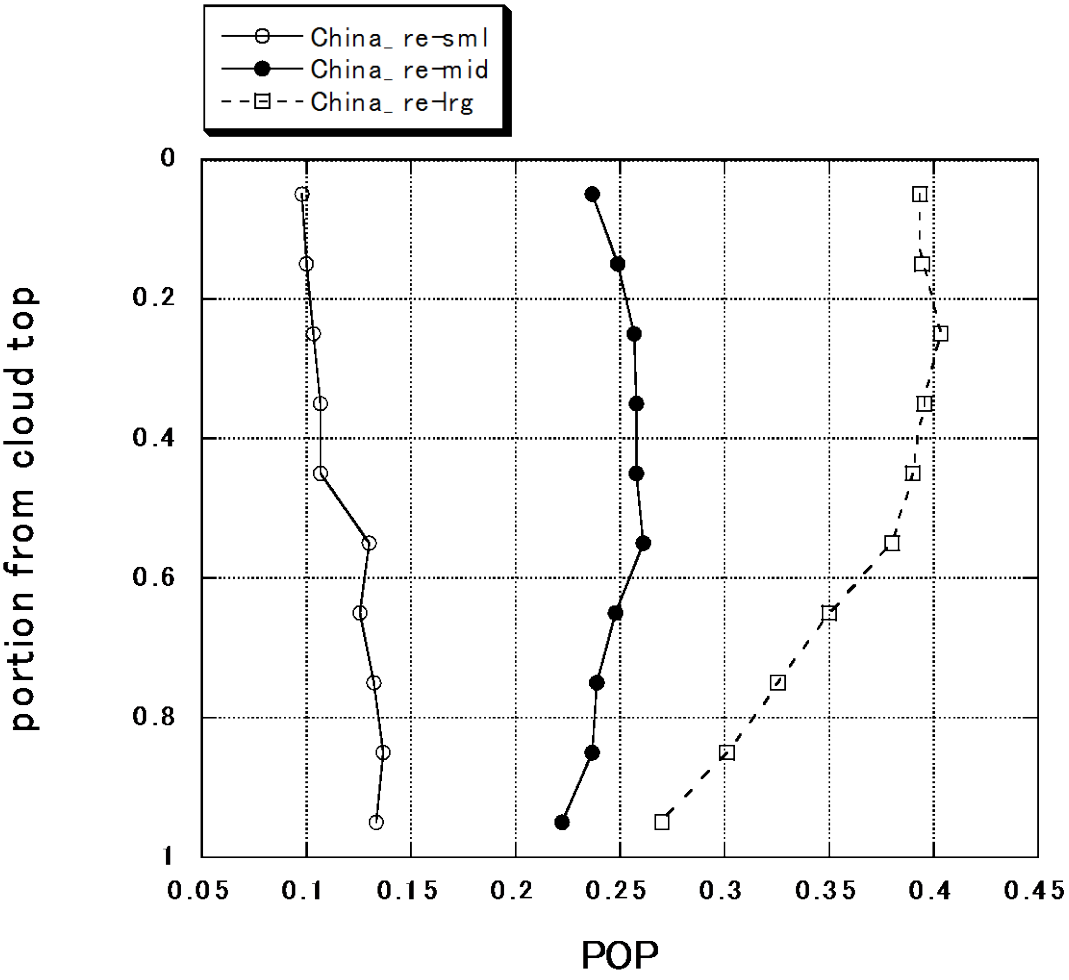
China_re-sml
China_re-mid
China_re-lrg
portion from cloud top
0
0.2
0.4
0.6
0.8
1
0.05
0.1
0.15
0.2
0.25
0.3
0.35
0.4
0.45
POP

Figure 14 (b)

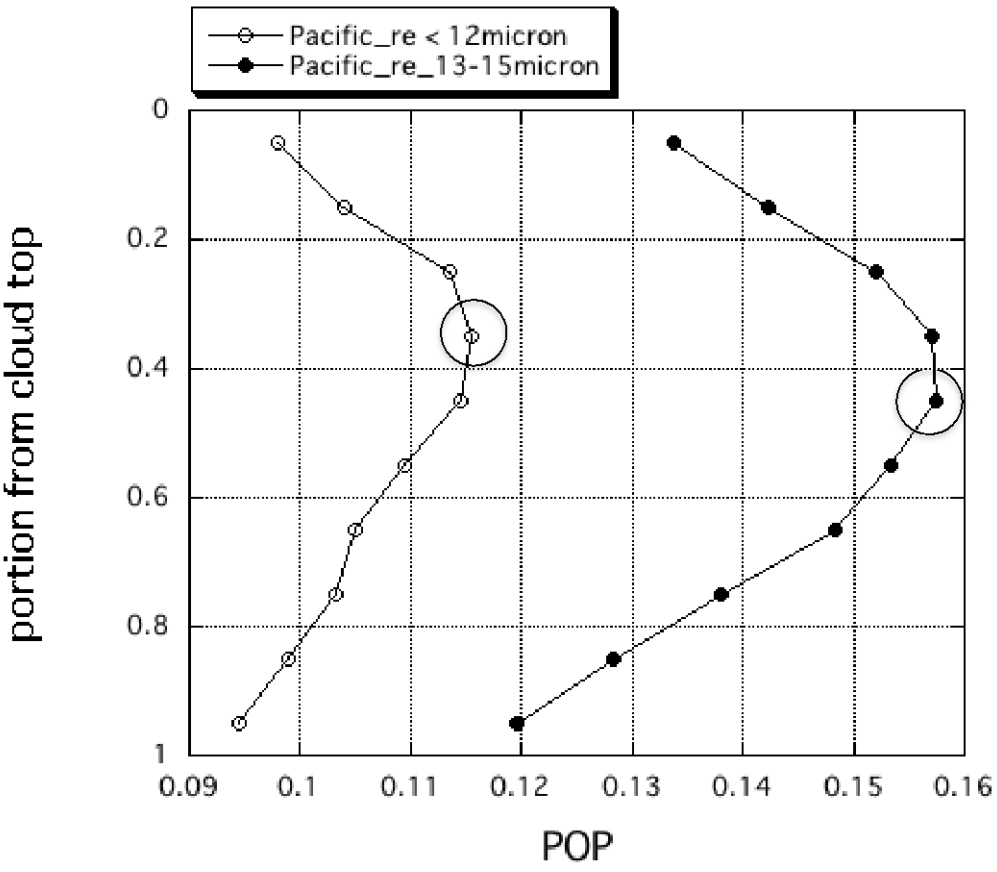
Pacific_re < 12micron
Pacific_re_13-15micron
portion from cloud top
0
0.2
0.4
0.6
0.8
1
0.09
0.1
0.11
0.12
0.13
0.14
0.15
0.16
POP

Figure 15

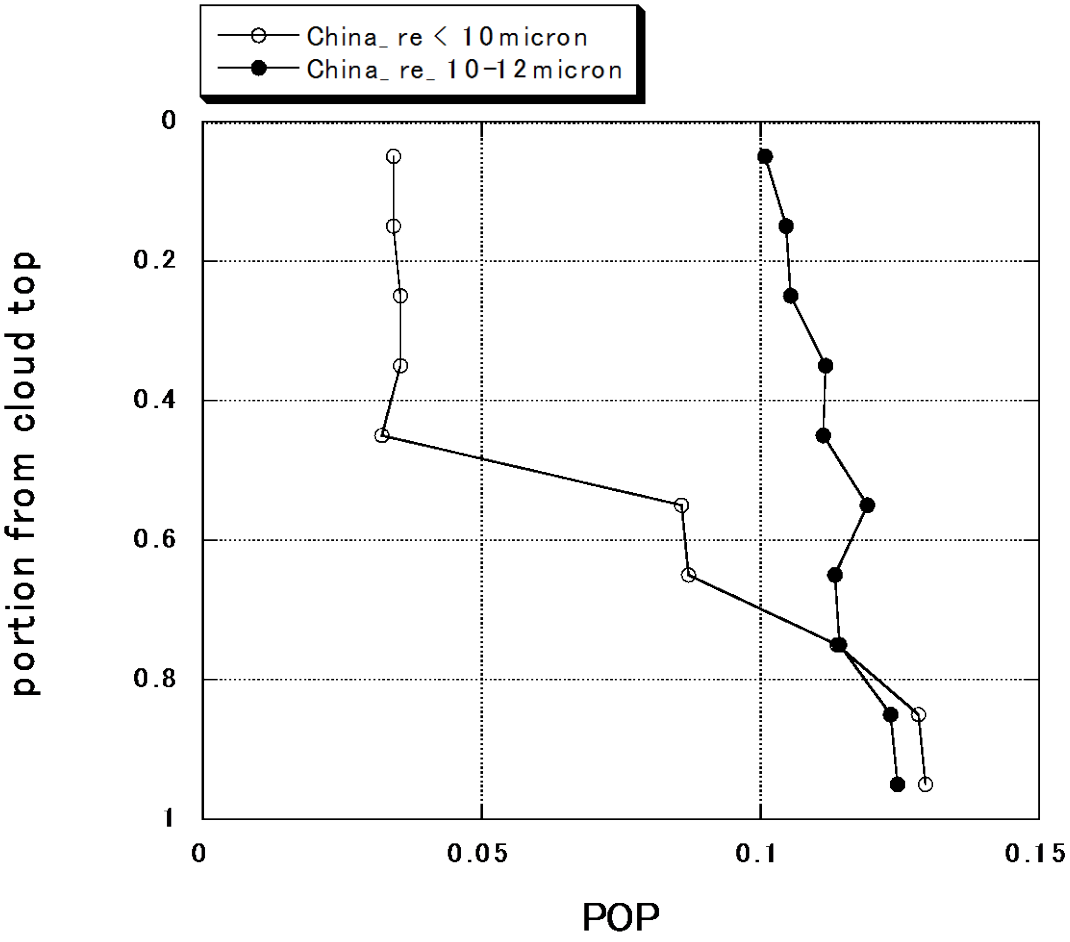
China_ re < 10micron
China_ re_ 10-12micron
portion from cloud top
0
0.2
0.4
0.6
0.8
1
0
0.05
0.1
0.15
POP

Figure 16.

Figure captions

Figure 1. Map of the areas analyzed in this study. The dotted and solid circles represent the northwestern Pacific and China, respectively.

Figure 2. The PDFs of r_e for the Pacific and China.

Figure 3. The PDFs of D_{cld} for the Pacific and China.

Figure 4. The PDFs of LWP for the Pacific and China.

Figure 5. The PDFs of Z_e for the Pacific and China.

Figure 6. The frequency distributions of maxZ_e according to the three categories of r_e for (a) the Pacific and (b) China.

Figure 7. The frequency distributions of maxZ_e according to the three categories of D_{cld} for (a) the Pacific and (b) China.

Figure 8. The frequency distributions of maxZ_e according to the three categories of LWP for (a) the Pacific and (b) China.

Figure 9. The PDFs of r_e according to the three categories of LWP for (a) the Pacific and (b) China.

Figure 10. The frequency distributions of maxZ_e according to the three categories of r_e in the sml category of LWP for (a) the Pacific and (b) China.

Figure 11. Scatterplot on the r_{e_mw} ratio diagram proposed by Masunaga et al. (2002) for the Pacific. The four subgroups are indicated in terms of r_e and the ratio. Red and blue circles have ratios greater than 1 and less than 1, respectively.

Figure 12. The frequency distributions of maxZ_e according to the subgroups for the Pacific.

Figure 13. The frequency distributions of D_{cld} according to the subgroups for the Pacific.

Figure 14. The vertical profiles of the POP for the scaled cloud layer according to the three categories of r_e for (a) the Pacific and (b) China.

Figure 15. The vertical profiles of the POP for the scaled cloud layer according to the two ranges of r_e (less than 12 μm, between 13 and 15 μm) for Pacific.

Figure 16. The vertical profiles of the POP for the scaled cloud layer according to the two ranges of r_e (less than 10μm, between 10 and 12μm) for China.